

A light-weight NO₂-to-NO_x conversion model for quantifying NO_x emissions of point sources from NO₂ satellite observations

Sandro Meier^{1,2}, Erik F. M. Koene¹, Maarten Krol^{3,4}, Dominik Brunner¹, Alexander Damm^{2,5}, and Gerrit Kuhlmann¹

¹Empa, Laboratory for Air Pollution / Environmental Technology, Ueberlandstrasse 129, 8600 Duebendorf, Switzerland

²Department of Geography, University of Zurich, Winterthurerstrasse 190, 8057 Zurich, Switzerland

³Meteorology and Air Quality, Wageningen University & Research, Wageningen, The Netherlands

⁴Institute for Marine and Atmospheric Research Utrecht (IMAU), Utrecht University, The Netherlands

⁵Eawag, Swiss Federal Institute of Aquatic Science & Technology, Surface Waters – Research and Management, Ueberlandstrasse 133, 8600 Duebendorf, Switzerland

Correspondence: Sandro Meier (sandro.meier@empa.ch), Gerrit Kuhlmann (gerrit.kuhlmann@empa.ch)

Abstract.

Nitrogen oxides (NO_x = NO + NO₂) are air pollutants which are co-emitted with CO₂ during high-temperature combustion processes. Monitoring NO_x emissions is crucial for assessing air quality and for providing proxy estimates of CO₂ emissions. Satellite observations, such as those from the TROPOspheric Monitoring Instrument (TROPOMI) on board the Sentinel-5P satellite, provide global coverage at high temporal resolution. However, satellites measure only NO₂, necessitating a conversion to NO_x. Previous studies applied a constant NO₂-to-NO_x conversion factor. In this paper, we develop a more realistic model for NO₂ to NO_x conversion and apply it to TROPOMI data of 2020 and 2021. To achieve this, we analysed plume-resolving simulations from the MicroHH Large Eddy Simulation model with chemistry for the power plants Bełchatów (PL), Jänschwalde (DE), Matimba and Medupi (ZA), as well as a metallurgical plant in Lipetsk (RU). We used the cross-sectional flux method to calculate NO, NO₂ and NO_x line densities from simulated NO and NO₂ columns and derived NO₂-to-NO_x conversion factors as a function of the time since emission. Since the method of converting NO₂ to NO_x presented in this paper assumes steady state conditions as well as that the conversion factors can be modeled by a negative exponential function, we validated the conversion factors using the same MicroHH data. Finally, we applied the derived conversion factors to TROPOMI NO₂ observations of the same sources. The validation of the NO₂-to-NO_x conversion factors shows that they can account for the NO_x chemistry in plumes, in particular for the conversion between NO and NO₂ near the source and for the chemical loss of NO_x further downstream. When applying these time-since-emission-dependent conversion factors, biases in NO_x emissions estimated from TROPOMI NO₂ images are greatly reduced from between -50 and -42% to only -9.5 to -0.5% in comparison with reported emissions. Single-overpass estimates can be quantified with an uncertainty of 20–27%, while annual NO_x emission estimates have uncertainties in the range of 4–21% but are highly dependent on the number of successful retrievals. Although more simulations covering a wider range of meteorological and trace gas background conditions will be needed to generalize the approach, this study marks an important step towards a consistent, uniform, high-resolution, and near real-time

estimation of NO_x emissions - especially with regard to upcoming NO_2 monitoring satellites such as Sentinel-4 and -5 and CO2M.

1 Introduction

25 Nitrogen oxides ($\text{NO}_x = \text{NO} + \text{NO}_2$) are reactive trace gases and important air pollutants since they cause oxidative stress when respired, are involved in the formation of ground-level ozone (O_3) and particulate matter and contribute to acid rain (Thurston, 2017). As most NO_x emissions originate from high-temperature combustion processes, monitoring these sources is crucial for air quality regulation and can be used to estimate the (co-emitted) CO_2 emissions, provided that one knows the $\text{CO}_2:\text{NO}_x$ emission ratio for a given source (e.g., Goldberg et al., 2019a; Kuhlmann et al., 2021; Liu et al., 2020; Reuter et al., 30 2019; Hakkarainen et al., 2023). Estimating CO_2 emissions from large sources such as power plants and cities will be an important component of the CO_2 Monitoring and Verification Support (CO2MVS) service that is currently being developed under the European Copernicus CO_2 project (CoCO2) in support of the Paris Agreement (Pinty et al., 2017; Janssens-Maenhout et al., 2020). For this purpose, emission data should be available in near real time. A convenient method to obtain such high-resolution, uniform consistent emission estimates is to use satellite observations (Pinty et al., 2017).

35 Several case studies have investigated the potential and limitations of quantifying point source CO_2 emissions from space (e.g., Bovensmann et al., 2010; Goldberg et al., 2019b; Kuhlmann et al., 2021; Nassar et al., 2017; Reuter et al., 2019). One of the methods to quantify emissions is the cross-sectional flux method, which determines emissions by dividing a plume into several cross-sections. By integrating the measured vertical column densities along a cross-section, a line density is obtained. Each line density can be converted into a flux by multiplication with an effective wind speed representing the mean transport 40 speed of the plume. Under the assumption of steady-state conditions, the flux at each cross-section along the plume can be used to estimate the emissions (Varon et al., 2018).

Estimating CO_2 emissions from NO_2 satellite data is appealing because local NO_2 enhancements can be measured with higher accuracy than for CO_2 . There are also a number of existing and upcoming satellites that provide NO_2 products with high temporal and spatial coverage in comparison with CO_2 satellites. The most prominent existing instrument is the TROPospheric 45 Monitoring Instrument (TROPOMI) on the Sentinel-5 Precursor satellite, which provides daily observations of NO_2 and other trace gases with a spatial resolution of $3.5 \times 5.5 \text{ km}^2$ at nadir (van Geffen et al., 2022; Veeffkind et al., 2012). Several case studies have shown that TROPOMI data can be used to estimate NO_x emissions from cities and power plants (e.g., Douros et al., 2023; Goldberg et al., 2019b; Lorente et al., 2019).

Satellite-based radiance data only allow for the retrieval of NO_2 but not NO . However, more than 90% of NO_x from combustion processes is emitted as NO , which is then partially oxidized to NO_2 inside the plume (Pronobis, 2020; Seinfeld and Pandis, 2016). To retrieve NO_x emissions, it is therefore necessary to convert the measured NO_2 quantities to NO_x . Previous studies often used a constant NO_2 -to- NO_x conversion factor of about 1.32 derived assuming steady-state conditions (e.g., 50 Beirle et al., 2011; de Foy et al., 2015; Kuhlmann et al., 2021; Beirle et al., 2021). Recent studies that used regional chemistry transport model simulations derived spatially varying conversion factors in the range of 1.1 to 1.9, but acknowledge that the

55 values near sources are likely larger (e.g., Lorente et al., 2019; Rey-Pommier et al., 2022; Goldberg et al., 2022; Lange et al., 2022; Hakkarainen et al., 2024).

To study the NO_2 -to- NO_x conversion factor inside plumes, plume-resolving large eddy simulations of atmospheric transport with chemistry are necessary. In the CoCO2 project such simulations were conducted using the MicroHH model (van Heerwaarden et al., 2017; Krol et al., 2024). These simulations are described in further detail in Section 2.1.2. They showed that
60 the NO_x : NO_2 ratios inside the plume are highest near the source and decrease roughly exponentially with increasing time after emission (Krol et al., 2024). Figure 1 schematically depicts the evolution of NO, NO_2 and NO_x concentrations in a plume. While more than 90% of NO_x is emitted as NO (Pronobis, 2020), it is rapidly oxidised to NO_2 in the presence of ozone (O_3), titrating the available O_3 . Only after dilution and mixing of the plume with ambient air along the plume, the concentration of O_3 starts to increase again, leading to the oxidation of further NO. As a result, the ratio of NO_x to NO_2 is largest shortly
65 after the emission and gradually decreases over time. The rate of this oxidation process depends on several factors such as the amount of NO_x emitted, the concentration of O_3 and volatile organic compounds (VOCs), as well as photolysis rates and meteorological conditions. Subsequently, NO_2 is mainly removed by reacting with OH radicals with lifetimes ranging from hours to a few days in the lower troposphere (Seinfeld and Pandis, 2016). According to figure 1, NO_x decays exponentially with a constant e-folding lifetime, but in reality the lifetime may change along the plume due to changing OH radical concentrations.

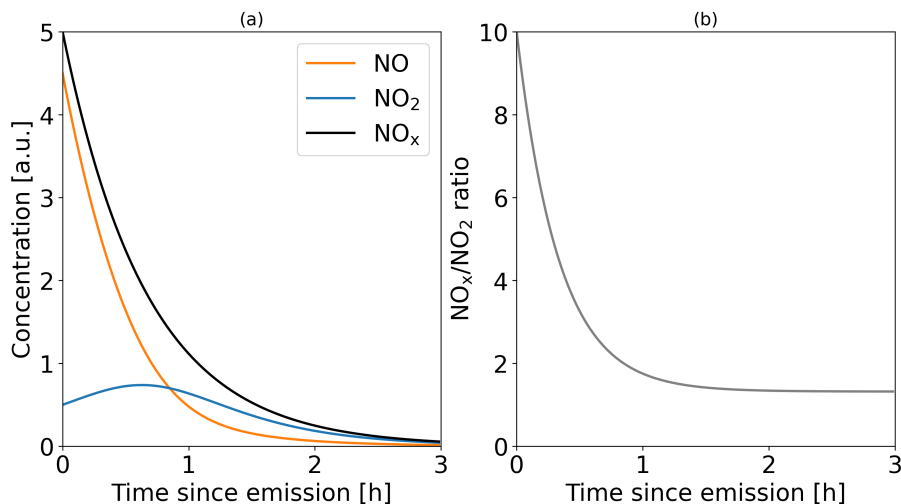


Figure 1. (a) Schematic illustration of NO, NO_2 and NO_x concentrations after the emission of NO_x where 90 % of NO_x is emitted as NO. (b) Resulting NO_x/NO_2 ratio.

70 Since the NO_x : NO_2 ratio inside plumes cannot be assumed constant, the aim of this study is to develop a more realistic model for a NO_2 -to- NO_x conversion factor that accounts for the spatiotemporal variations of NO_x chemistry in plumes. The model is applied in combination with the cross-sectional flux (CSF) method, which were both implemented in the Python package for “data-driven emission quantification” (see Section 2.1.1) (Kuhlmann et al., 2024, *ddeg*). To develop a more realistic conversion of NO_2 to NO_x that varies with time since emission and hence with the distance of the cross-section from the source, we use

75 MicroHH simulations that were conducted within the CoCO2 project. Simulations were performed for the power plants in Bełchatów (PL), Jänschwalde (DE) and Matimba & Medupi (ZA) (hereafter referred to as Matimba), as well as a metallurgical plant in Lipetsk (RU). The derived parameterisation is then applied to TROPOMI observations of these four sources over a two-year period.

2 Data and Methods

80 2.1 Development of a NO₂-to-NO_x conversion model using MicroHH simulations

2.1.1 Estimating emissions with the cross-sectional flux method

The CSF method is a common mass-balance approach, which can be used to estimate emissions of point sources. An implementation of the approach is available in the open-source Python library for data-driven emission quantification (ddeg; Kuhlmann et al. (2024)). Since the CSF method divides a plume into several cross-sections perpendicular to the plume direction and 85 establishes a plume-following coordinate system with along-plume and across-plume coordinates, it is ideal for studying the progress of the NO_x chemistry inside of the plume.

Figure 2 shows the application of the CSF method for a TROPOMI NO₂ image containing the plume from the Matimba and Medupi power plants in South Africa. Note that the power plants are only 6 km apart, so that their plumes appear as a single plume in the TROPOMI image. In a first step, a plume detection algorithm is used to determine the location of the 90 plume (Kuhlmann et al., 2019). A center line is drawn along the ridge of the plume, which is used to compute along- and across-plume coordinates (denoted by x and y , respectively), and to outline the plume area (yellow polygon in Fig. 2a). The polygon is subdivided in sub-polygons of 12 km length (Kuhlmann et al., 2020). For each sub-polygon, the mass of the trace gas enhancement over the background $\Delta\Omega$ [g m⁻²] is integrated over the width of the plume which yields line densities q [g m⁻¹] at distance x :

$$95 \quad q(x) = \int_{y_{min}}^{y_{max}} \Delta\Omega(x, y) dy \quad (1)$$

The plume width is defined as twice the maximum distance of a detected plume pixel from the center of the curve. As an alternative, the line density q can be computed by fitting a Gaussian curve to the enhancements inside the polygon, perpendicular to the direction of the plume:

$$g(y) = \frac{q}{\sqrt{2\pi}\sigma} \exp\left(-\frac{(y-\mu)^2}{2\sigma^2}\right) \quad (2)$$

100 with g being the fitted column using the standard width σ and center position μ to the observations (Kuhlmann et al., 2021). Figure 2b shows the computation of the line densities for six examples at different distances from the plume. The line densities computed from NO₂ observations at different distances from the source need to be converted to NO_x line densities using a NO₂-to-NO_x conversion model f that depends on the time since emission t :

$$q_{NO_x}(t) = f(t) \cdot q_{NO_2}(t) \quad (3)$$

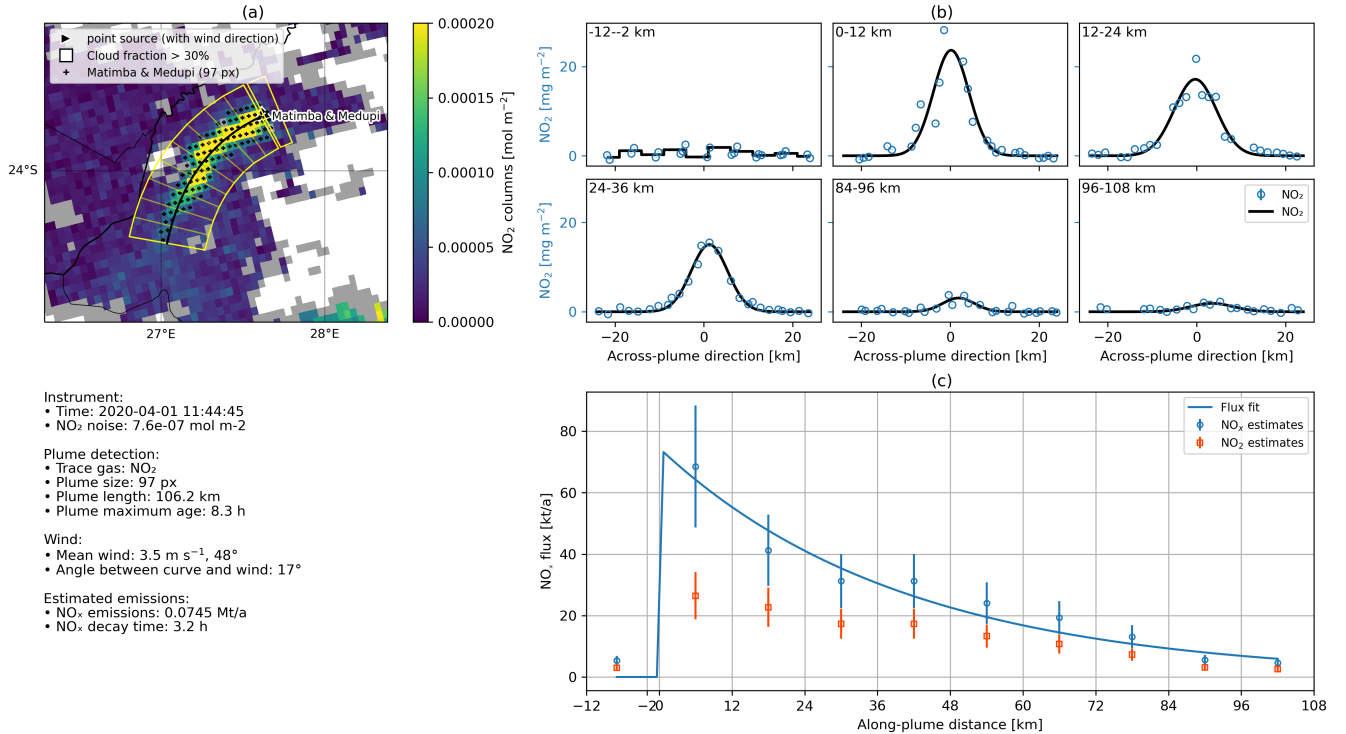


Figure 2. Example of the cross-sectional flux method. (a) Satellite image of a NO₂ plume divided into sub-polygons. (b) Integrated trace gas concentration for six sub-polygons. For downstream polygons, Eq. 2 is used. For the upstream polygon, the gas columns are summed up. (c) Estimated trace gas fluxes as mass NO₂ along the plume and the corresponding fitted function to estimate the emissions.

105 The time since emission t is computed from an effective wind speed u_{eff} at the source and the arc length of the center line (see Section 4.3). Details of the estimation of the function $f(t)$ are presented in Section 2.1.3.

Finally, the line densities are converted to fluxes F by multiplying them with u_{eff} . Finally, the emission Q is estimated by fitting a negative exponential function to the fluxes $F(t)$, the additional fit parameter τ representing the NO_x lifetime:

$$F(t, \tau) = Q \cdot \exp\left(-\frac{t}{\tau}\right). \quad (4)$$

110 Figure 2c shows how NO_x and NO₂ fluxes evolve with distance from the source. Note that the decrease of the flux is caused by the NO_x lifetime τ , while the NO₂-to-NO_x conversion model f is the ratio of the two lines.

2.1.2 Synthetic Satellite Observations

We use high-resolution atmospheric transport simulations with chemistry to simulate the NO_x and NO₂ concentrations inside plumes and to gain a better understanding of the NO_x:NO₂ ratios in plumes. For this study, we used simulations from the

115 MicroHH large eddy simulation (LES) (van Heerwaarden et al., 2017), which was recently extended with a chemistry module (Krol et al., 2024).

The simulations used are part of the library of plumes generated in the CoCO₂ project, where different models were used to simulate the plumes of point sources (Krol and van Stratum, 2021; Koene and Brunner, 2022). For the library, MicroHH was run on a 128 × 128 × 4 km domain in the longitude, latitude and altitude directions respectively for Matimba and a 51.2 × 51.2 × 4 km domain for Bełchatów, Jänschwalde, and Lipetsk. The spatial resolution was set to 100 × 100 × 25 m for the Matimba case and 50 × 50 × 25 m for the others. Each case was simulated for 48 hours, starting at 00:00 UTC, and the output was saved hourly. The simulation periods were selected based on the availability of measurements from aircraft campaigns and cloud-free TROPOMI images.

MicroHH simulates reactive trace gases and CO₂ as well as meteorological variables such as temperature, pressure, and wind speed. The model includes a simplified version of the chemistry scheme implemented in the IFS model of the European Centre for Medium Range Weather Forecast (Huijnen et al., 2016), simulating the species O₃, NO, NO₂, NO₃, N₂O₅, HNO₃, CO, CO₂, CH₄ (fixed), H₂ (fixed), HO₂, OH, H₂O₂, CH₂O, RO₂, and ROOH, as well as C₃H₆ as a representative of VOCs. The chemistry was tuned to match the NO_x and HO_x chemistry of IFS and to realistically represent the photostationary state between NO, NO₂ and O₃. The model was initialised and driven with hourly meteorological data from the ERA5 reanalysis. For the background concentrations of trace gases, reanalysis data from the Copernicus Atmosphere Monitoring Service (CAMS) were used (Krol et al., 2024; van Stratum et al., 2023). To simulate the plumes, typical quantities of NO_x emissions from bottom-up reported values of previous years were released at the respective locations of the power plants and industrial facilities. The NO_x emissions were split into 95% NO and 5% NO₂ by mass (Krol and van Stratum, 2021).

Table 1. Details of the four MicroHH simulations used in this study. Additional details can be found in (Krol et al., 2024)

Facility	Country	Simulation period	Simulated emissions [kg s ⁻¹]
Power plant Jänschwalde	Germany	22 - 23 May 2018	0.6021
Power plant Bełchatów	Poland	6 - 7 June 2018	0.9538
Steel plant Lipetsk	Russia	12 - 13 June 2019	0.8302
Power plant Matimba and Medupi	South Africa	24 - 25 July 2020	2.4920

The model output consisted of 3D data of the reactive trace gases as well as meteorological variables such as temperature, pressure, and wind speed. The output was post-processed into 2D datasets resembling synthetic satellite observations but without including any measurement noise. The resolution was degraded to the expected resolution of the CO2M satellites of 2 × 2 km. For the wind speeds, a 2D weighted average of the 3D wind fields was calculated based on the vertical emission profile. The temporal evolution of wind speeds, background concentrations and photolysis rates is displayed in Figures S1, S2 and S4 the supplement. These wind speeds are used to estimate the simulated emissions. The specific model settings and boundary conditions used for the MicroHH model runs are described in Krol and van Stratum (2021) and Krol et al. (2024) while the post-processing is documented in Koene and Brunner (2023).

2.1.3 Conversion of NO₂ to NO_x line densities in MicroHH

To derive a more realistic conversion model of NO₂ to NO_x line densities $f(t)$, the vertically integrated MicroHH simulations were analysed for the sources Bełchatów, Jänschwalde, Lipetsk, and Matimba by applying the CSF method as outlined above.

145 We analysed the time steps 8 to 14 UTC for both simulated days instead of only the ones at TROPOMI overpass time to derive more robust NO₂-to-NO_x conversion factors that better represent varying atmospheric and site conditions. For each polygon of the detected plumes, the line densities of NO and NO₂ were calculated. The along-plume distance of each plume was divided by the profile-weighted wind speed at the source to convert them to a time since emission. Such a conversion allows us to account for the effects of varying wind speeds on the concentration of trace gases. For each source, we fitted a negative
150 exponential function to the median NO_x:NO₂ ratio, using the standard deviations of the analysed time steps as uncertainties.

$$f(t) = m \cdot \exp(-r \cdot t) + f_0 \quad (5)$$

The fitting parameter m represents a scaling factor, r the rate at which the NO_x:NO₂ ratio decreases and f_0 the offset to which the ratio will converge to with time. A negative exponential function was chosen for the conversion of NO₂ to NO_x to account for the initial increase in NO₂ due to the oxidation of NO. The resulting conversion factor $f(t)$ can be multiplied with the
155 corresponding $q_{\text{NO}_2}(t)$ line densities to obtain $q_{\text{NO}_x}(t)$. The uncertainty σ_f of f is calculated from the fitted uncertainties of the three parameters by propagation of uncertainty

$$\sigma_f(t) = \sqrt{\left(\frac{\partial f(t)}{\partial m}\right)^2 \sigma_m^2 + \left(\frac{\partial f(t)}{\partial r}\right)^2 \sigma_r^2 + \left(\frac{\partial f(t)}{\partial f_0}\right)^2 \sigma_{f_0}^2} \quad (6)$$

and used to update the uncertainty σ_l of the NO_x line densities q :

$$\sigma_q = \sqrt{f^2 \sigma_q^2 + \sigma_f^2 q^2} \quad (7)$$

160 The method of converting NO₂ to NO_x presented in this paper relies on the assumption of steady state conditions as well as an exponential decay of the conversion factor (Eq. 5). Therefore, it is important to check if NO_x emission estimates derived from the time-dependent algorithm are consistent with the emitted quantities. For this purpose, we estimated the NO_x emissions of the same daytime time steps of MicroHH three times: once using the modelled NO_x fields, once using the NO₂ fields and applying the constant NO₂-to-NO_x conversion factor of 1.32 (referred to as the algorithm with constant factor), and once using
165 the negative exponential function fitted above as conversion factors (referred to as the time-dependent algorithm).

2.2 Application to TROPOMI NO₂ satellite observations

2.2.1 TROPOMI Satellite Observations

We applied the method of converting NO₂ to NO_x line densities developed in the current study to the latest processing version (v2.4.0) of the tropospheric NO₂ observations from TROPOMI for the years 2020 and 2021. In accordance with van Geffen
170 et al. (2019), only data with quality assurance values higher than 0.75 were utilised. In addition, we downloaded the auxiliary

data comprising 3D NO₂ fields from the 3D chemistry-transport model TM5-MP to recompute the air mass factors (AMFs) (see Section 2.2.2) (Eskes and van Geffen, 2021)). To determine the NO₂ line densities, we fit a Gaussian curve (Eq. 2) to the observed NO₂ VCDs using a weighted least squares (WLS) method. Since the errors in NO₂ VCDs depends on the retrieved VCDs, computing the weights from the reported errors would give lower weight to higher VCDs and, as a result, would tend to
 175 underestimate the line density. To avoid this, we set the precision of the retrieved tropospheric NO₂ vertical column densities (VCDs) to $7.6 \cdot 10^{-7} \text{ kg m}^{-2}$, which corresponds to $1 \cdot 10^{-15} \text{ molecules cm}^{-2}$. This is an average uncertainty over polluted regions and corresponds to approximately 20% of the measured NO₂ VCDs (van Geffen et al., 2019).

Emissions were estimated by applying the constant and time-dependent algorithms to the AMF-corrected images. For each source, the respective fitting parameters m , r and f_0 from the MicroHH simulations were used to convert NO₂ into NO_x.
 180 Estimates were then aggregated by month and annual emissions were estimated as the median of the monthly statistics. This was done to avoid a potential bias due to an unbalanced number of data points per month. For estimating the uncertainty of the annual emissions, a seasonal cycle was fitted to all emission estimates using a cubic Hermite spline with periodic boundary conditions (Kuhlmann et al., 2021). The corresponding uncertainty σ_e accounts for the uncertainties of the single-overpass estimates through error propagation. To further account for uncertainties in the diurnal (σ_d) and seasonal (σ_s) cycles, the total
 185 uncertainty σ_{tot} was calculated as follows:

$$\sigma_{\text{tot}} = \sqrt{\sigma_e^2 + \frac{\sigma_d^2}{n} + \frac{\sigma_s^2}{n}} \quad (8)$$

Here, both σ_d and σ_s were set to 30% according to Hill and Nassar (2019). As the estimated NO_x emissions with the time-dependent algorithm depend on the NO₂-to-NO_x conversion factor, a sensitivity analysis was performed by applying the NO₂-to-NO_x conversion factors calculated for Janschwalde and Matimba to all four sources.

190 2.2.2 Air mass factor correction

For the retrieval of NO₂ VCDs, a priori NO₂ profiles from a 3D chemistry transport simulation called TM5-MP are used. Due to its coarse resolution of $1^\circ \times 1^\circ$, the model cannot resolve individual plumes but rather represents them as smeared out NO₂ enhancements. Consequently, the TM5-MP pixels have neither the correct concentration profile of the plume nor the correct background concentration. This tends to lead to an overestimation of AMFs and consequently an underestimation of VCDs
 195 within the observed plumes and, vice versa, outside of the plumes. Such a bias over polluted regions is known from previous studies (Griffin et al., 2019; Verhoelst et al., 2021; Douros et al., 2023). To address these biases we constructed a more realistic NO₂ profile that is representative for the observed plumes. To this end, we interpolated the auxiliary data from the TM5-MP model and the ERA5 planetary boundary layer (PBL) height data to the higher resolution TROPOMI pixels. We set the NO₂ mole fraction within the PBL to $5 \cdot 10^{-9} \text{ mol/mol}$ for all detected plume pixels of the images for the years 2020 and 2021.
 200 This is an average NO₂ concentration within the PBL of detected plumes based on the four MicroHH simulations, independent of the along-plume distance. However, we acknowledge that the profile concentration should ideally decrease along the plume.

With the new NO₂ profiles x_{new} , we recalculated the AMFs according to Eskes et al. (2022):

$$\text{AMF}_{new}(x_{new}) = \text{AMF}_{old}(x_{old}) \cdot \frac{\sum_l A_l \cdot x_{new,l}}{\sum_l x_{new,l}}. \quad (9)$$

Finally, we updated the VCDs inside the detected plumes for all images using the recalculated AMF_{new}:

$$205 \quad \text{VCD}_{new} = \frac{\text{VCD}_{old} \cdot \text{AMF}_{old}}{\text{AMF}_{new}} \quad (10)$$

We only recalculated the AMFs and VCDs of detected plume pixels because no other anthropogenic sources other than the power plant or steel plant in focus were simulated by MicroHH. Thus, the NO_x concentrations were too low to obtain representative background concentrations.

2.2.3 ERA5 wind data

210 The CSF method requires wind data to convert trace gas line densities into fluxes. For this purpose, we weighted the 3D wind fields of the ERA5 reanalysis ((Hersbach et al., 2018)) with a profile representing the expected vertical distribution of emissions for power plants in Brunner et al. (2019) and integrated them vertically to obtain 2D wind fields. As in Kuhlmann et al. (2021), we assumed a fixed wind speed uncertainty of 1 m/s for the error propagation in the emission estimation.

2.2.4 Comparison with bottom-up reported NO_x emissions at high temporal resolution

215 Since the year 2000, member states of the European Union have been required to report the emissions of air and water pollutants from large point sources (European Parliament and the Council of the European Union). These data were made publicly available in 2006 through the European Pollutant Release and Transfer Register (E-PRTR). The database contains the annual emissions of pollutants from nine major sectors such as energy production or metal processing and is available on the European Industrial Emissions Portal (<https://industry.eea.europa.eu/>). We use the bottom-up reported emissions to assess the accuracy
220 of our emission estimates. We obtained data as annual NO_x emissions from the Jämschalde power plant for the years 2020 to 2021. For the Bełchatów power plant, the data are only available up to 2017. Therefore, we used the CO₂ and NO_x emissions for 2017 to extrapolate the expected emissions for the years 2020 to 2021 according to Nassar et al. (2022). For the metallurgical plant in Lipetsk, no accurate data on emissions were available since there are no bottom-up reported emissions for this specific
225 captive power plants at the Lipetsk site are included in the reported emissions. For the Matimba and Medupi power plants, monthly emissions are provided by the operating company Eskom.

For all three power plants, we interpolated the annual and monthly bottom-up reported CO₂ and NO_x emissions to hourly and daily temporal resolution by weighting them with the power plant's energy output according to Nassar et al. (2022). For the European power plants, we used the hourly electricity generation from the transparency platform of the European Network
230 of Transmission System Operators for Electricity (ENTSO-E) (<https://transparency.entsoe.eu/>). For the Matimba and Medupi power plants, we used the daily electricity production provided by the operating company Eskom.

3 Results

3.1 NO_x to NO_2 ratios in plumes

An example of the NO_2 and NO_x vertical column fields simulated with MicroHH for the Matimba case as well as the corresponding $\text{NO}_x:\text{NO}_2$ ratios is depicted in Figure 3. The spatiotemporal patterns of $\text{NO}_x:\text{NO}_2$ ratios of all simulations are displayed in Figure A1.

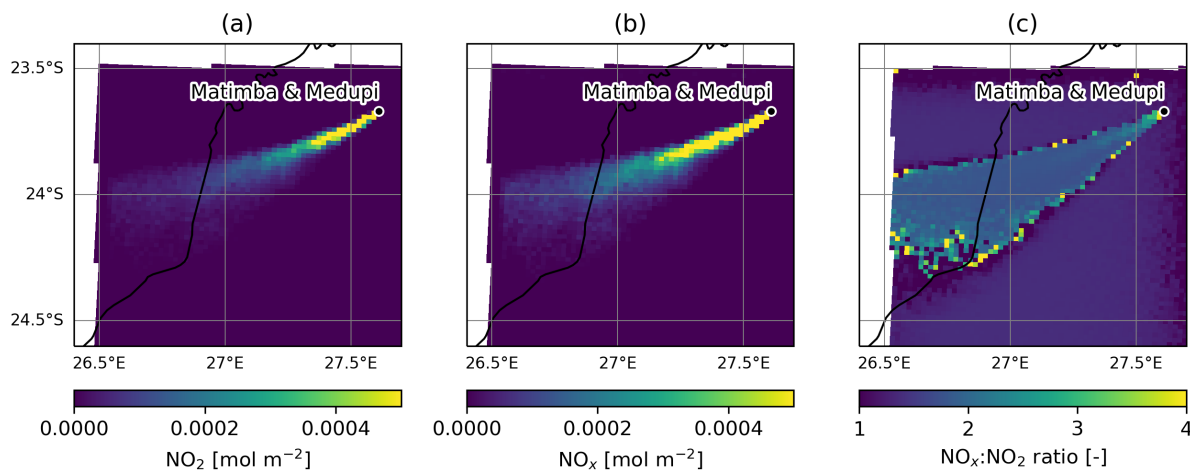


Figure 3. Simulated NO_2 (a) and NO_x (b) fields as well as the resulting $\text{NO}_x:\text{NO}_2$ ratios (c) from time step 32 (08:00 UTC) of the MicroHH simulation of Matimba.

The evolution of $\text{NO}_x:\text{NO}_2$ ratios in the MicroHH model as a function of time since emission is summarized in Figure 4 for all four cases Bełchatów, Jämschalde, Lipetsk, and Matimba. The figure contains results from all hourly time steps between 8 and 14 UTC from both simulated days.

Panel (a) shows the median and standard deviation of the ratios, while (b) depicts the corresponding fitted negative exponential functions and the fitted standard deviations. The figure confirms our expectation that the $\text{NO}_x:\text{NO}_2$ ratios are largest close to the source and decrease with increasing distance downwind. The ratios are generally much larger than the previously used conversion factor $f_0=1.32$ (black horizontal line) and only approach this value at distances larger than 50-100 km and only in some cases. Because most of the NO_x is emitted as NO, NO concentrations close to the source are very high, which leads to complete titration of O_3 present in background air and therefore limits the production of NO_2 through the oxidation of NO by O_3 . With increasing dilution and mixing of the plume with background air downwind of the source, the concentration of NO decreases while the concentration of O_3 increases. This accelerates the oxidation of NO and gradually shifts the photostationary equilibrium ratio of $\text{NO}:\text{NO}_2$ towards NO_2 and reduces the $\text{NO}_x:\text{NO}_2$ ratio accordingly (Seinfeld and Pandis, 2016). Compared to the other three simulations, the $\text{NO}_x:\text{NO}_2$ ratio of the Matimba simulation is higher both at the source and further downwind. The main reason for this behaviour is the amount of NO_x emitted: the more that is emitted, the longer it

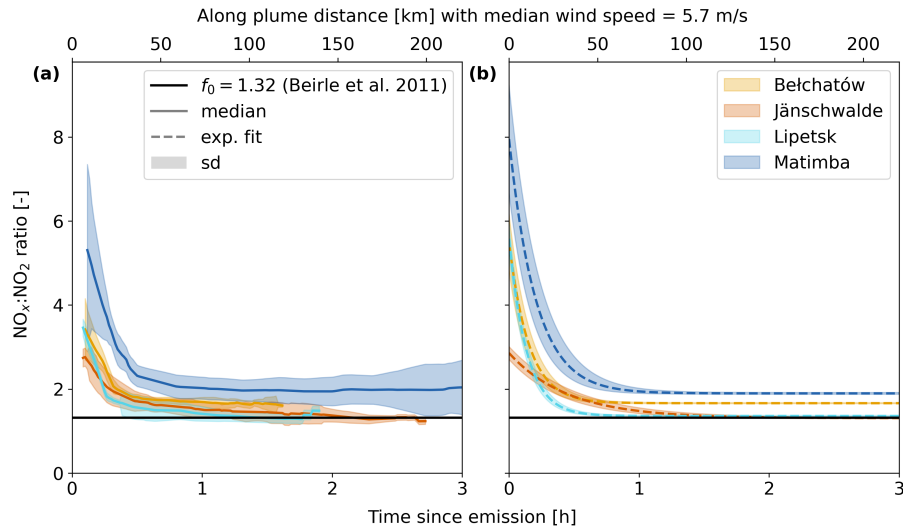


Figure 4. Mean $\text{NO}_x:\text{NO}_2$ ratios of the MicroHH time steps 8 – 14 UTC as a function of time since emission. (a) Median and standard deviation. (b) Fitted negative exponential function and corresponding standard deviation. The time axis is converted to a space axis using the median wind speed in all analysed plumes.

takes for the plume to mix in sufficient O_3 from the surrounding air masses to reach the background photostationary state for NO_x (Krol et al., 2024). Another reason for the different $\text{NO}_x:\text{NO}_2$ ratios are the meteorological conditions which determine how fast the plumes are mixed with surrounding air masses. Furthermore, the background concentrations of O_3 and VOCs that are different for all simulations have a strong influence on the $\text{NO}_x:\text{NO}_2$ ratios and partly explain the higher values of f_0 for Bełchatów and Matimba (see Figures S2, S3 and S4 in the supplement) (Seinfeld and Pandis, 2016). In all four simulations, the ratios level off half an hour after the emission or 50 km along the plume, assuming a median wind speed of the analysed time steps of about 5.7 m/s. Furthermore, Figure 4 illustrates that the standard deviation close to the source is largest for Bełchatów, which leads to a higher uncertainty in the fitted function. The corresponding fitting parameters of the $\text{NO}_x:\text{NO}_2$ ratios and their uncertainties are listed in Table 2.

Table 2. Fitting parameters of the negative exponential function in Eq. 5 to the mean $\text{NO}_x:\text{NO}_2$ ratios of the four MicroHH simulations for the steps 8 to 14 UTC.

Source	m [-]	$\frac{1}{\tau}$ [min]	f_0 [-]
Bełchatów	3.8 ± 0.7	9.1 ± 0.8	1.66 ± 0.01
Jänschwalde	1.6 ± 0.1	27.3 ± 2.7	1.31 ± 0.01
Lipetsk	4.2 ± 0.3	8.1 ± 0.4	1.36 ± 0.02
Matimba	6.1 ± 1.3	12.4 ± 1.4	1.90 ± 0.02

260 To convert NO_2 line densities into NO_x line densities, they are multiplied with $f(t)$ following Eq. (5). The results for the Matimba plume are shown in Figure 5. As a result of the multiplication, the NO_x line densities peak at the source and approximately follow an exponential decay similar to the schematic in Figure 1. In contrast, the NO_2 line densities peak between 20 to 30 km.

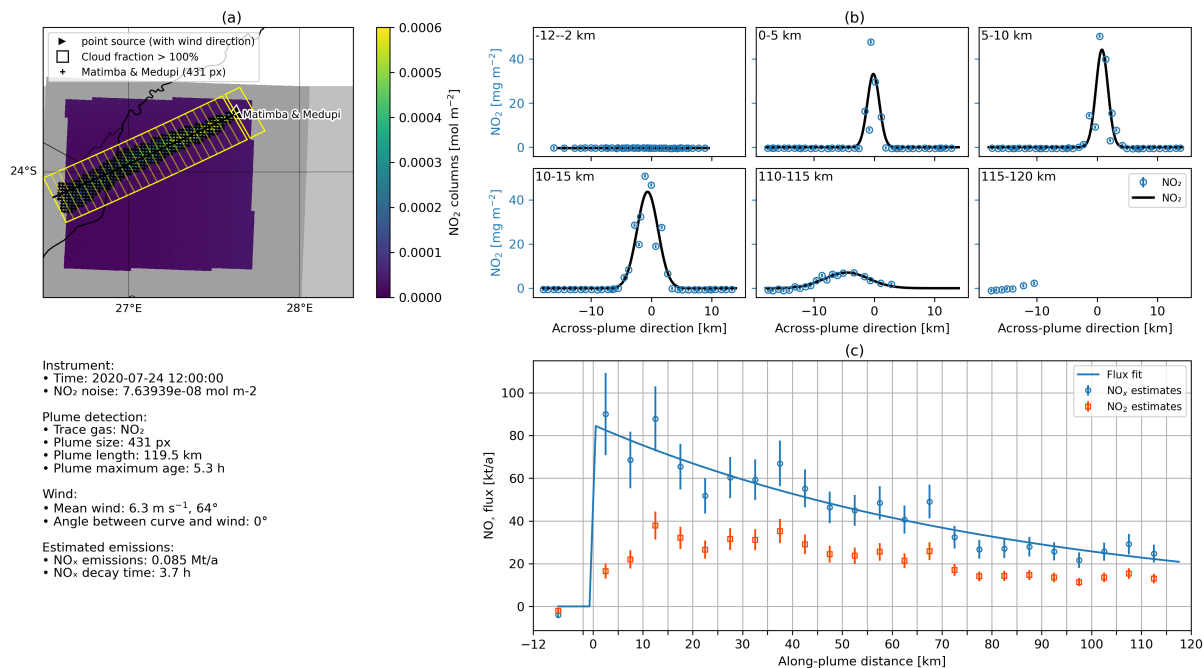


Figure 5. Example of estimating NO_x emissions from Matimba MicroHH simulation using the time-dependent conversion of NO_2 to NO_x for the cross-sectional flux method implemented in *ddeq*.

265 Applying the NO_2 -to- NO_x conversion factors to the MicroHH data as a validation in Figure 6 shows that the estimated NO_x emissions with the time-dependent algorithm are in good agreement with the estimates from the modelled NO_x fields. However, the spread of the estimates is larger when converting NO_2 to NO_x , which is due to the assumption that the conversion can be modelled by a negative exponential function. Furthermore, emissions estimated from the modelled NO_x fields should align with the prescribed emissions. However, the emissions are overestimated for Bełchatów and Jänschwalde and underestimated for Matimba, which is due to uncertainties of the CSF method (see Section 4).

270 Similar to the emission estimates, the estimated NO_x decay times using the time-dependent algorithm are more consistent with those from the modelled NO_x fields whereas the estimates using the algorithm with constant factor are more than twice as high. This overestimation with the algorithm with constant factor is due to the fact that NO_2 decreases less rapidly than NO_x due to the gradual shift in the $\text{NO}:\text{NO}_2$ photostationary equilibrium ratio towards NO_2 as mentioned earlier.

275 The improved agreement between the estimates from modelled NO_x fields and the time-dependent algorithm shows that this model of converting NO_2 to NO_x accounts for the NO_x chemistry in the plumes simulated by MicroHH quite well.

The larger discrepancies for Bełchatów and Jänschwalde compared to the other cases are probably due to the higher relative uncertainties of the fitted $\text{NO}_2:\text{NO}_x$ ratios as seen in Figure 4b. Nevertheless, the estimated emissions and lifetimes are a significant improvement over the approach of converting NO_2 to NO_x using a constant factor of 1.32.

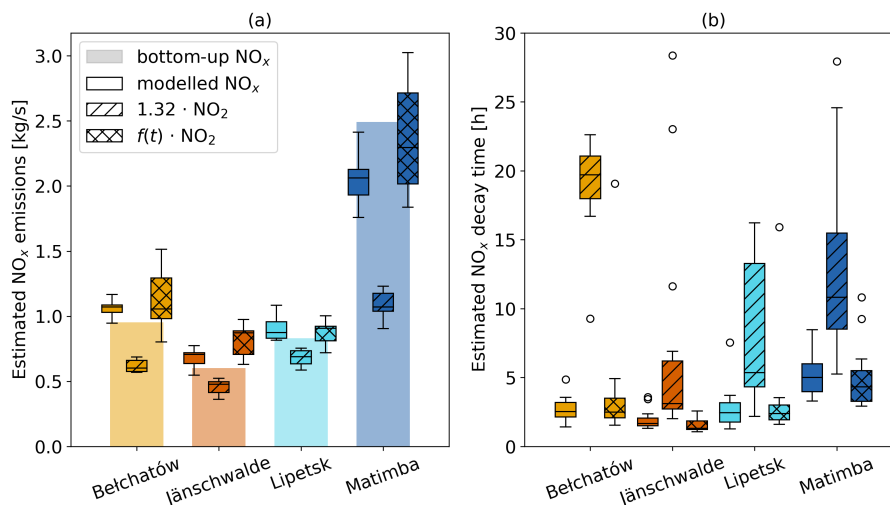


Figure 6. (a) Comparison of estimated NO_x emissions against the prescribed (bottom-up) emissions and (b) estimated NO_x decay times using the constant and time-dependent algorithms as well as the modelled NO_x fields. Only the daytime time steps of the MicroHH simulations were utilised. Boxes in the histograms represent the interquartile range (IQR, 25th to 75th percentile), whiskers the range between $Q1 - 1.5 \cdot \text{IQR}$ and $Q3 + 1.5 \cdot \text{IQR}$ and circles all data points that fall outside of this range.

3.2 Application of the conversion of NO_2 to NO_x to TROPOMI observations

280 For the years 2020 and 2021, a total of 737 TROPOMI images were available for Bełchatów, 807 for Jänschwalde, 862 for Lipetsk and 454 for Matimba. However, for the first three sources, only about 7% of the images were sufficiently cloud-free. For Bełchatów and Jänschwalde, the plume detection only worked for half of these cloud-free images due to the proximity to other coal-fired powerplants. As a result, the plumes often mixed, rendering the estimation of emissions impossible. For Matimba, almost half of the total available images were cloud-free, with plume detection working on more than 80% of these
 285 images due to the remote location. An example image of the emission estimation for TROPOMI can be seen in Figure 2.

The AMFs computed for the four cases result in a mean increase of the VCDs inside the plume by a factor of 1.11 – 1.35 (see Figure A2). The estimated NO_x emissions from the AMF-corrected TROPOMI data for the years 2020 and 2021 are presented in Figure 7 and listed in Table 3. While the emissions estimated with the algorithm with constant factor only amount to 48–69% of the bottom-up reported emissions, the emissions derived with the time-dependent algorithm are more in line and reach about
 290 88–109%. For all four sources, these estimates are within one standard deviation of the bottom-up reported emissions.

Figure 7 also shows that the range of estimated emissions is largest for Matimba with a large number of outliers. The most likely explanation is that the plumes are the longest for this source, meaning that parts of the plume are several hours old and

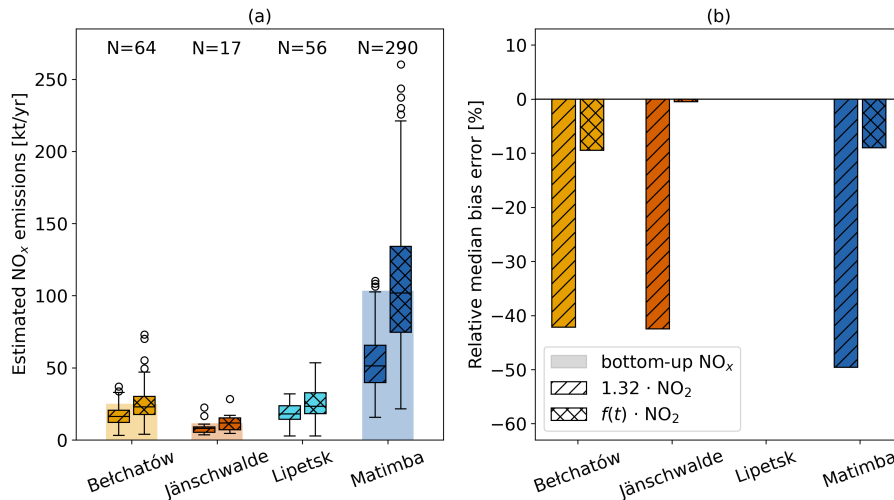


Figure 7. (a) Estimated NO_x emissions and (b) their median bias errors relative to the bottom-up reported emissions for Bełchatów, Jänschwalde, Lipetsk, and Matimba for TROPOMI data of the years 2020 and 2021.

have likely been subject to different chemistry and wind speeds (see Fig. A6). This leads to strong violations of the assumed steady-state conditions along the plume and results in outliers in the NO_x fluxes along the plume. The relative mean bias error of a given method is in a similar range for all four sources. While the bias is around -50% relative to the bottom-up reported emissions with the algorithm with constant factor, it is reduced to only -9.5 to -0.5% with the time-dependent algorithm.

Table 3. Median and standard deviation of estimated NO_x emissions in kt NO₂/a for the years 2020 and 2021 for Bełchatów, Jänschwalde, Lipetsk, and Matimba derived from TROPOMI images

Source	$1.32 \cdot \text{NO}_2$	$f(t) \cdot \text{NO}_2$	Bottom-up
Bełchatów	14.6 ± 4.2	22.0 ± 8.2	25.1
Jänschwalde	8.0 ± 0.7	12.7 ± 1.9	11.6
Lipetsk	18.4 ± 4.1	23.4 ± 6.8	–
Matimba	49.2 ± 16.6	104.2 ± 45.8	103.4

The uncertainties of the single-overpass and annual estimates are listed in Table 4. The first column shows the median uncertainty of all single-overpass estimates. The second column represents the standard deviation of the difference between estimated and bottom-up emissions. The uncertainties of the first column would agree with those in the second if the bottom-up reported emissions corresponded to the true emissions and all uncertainties were included in the emission estimation. However, the larger magnitude of the values in the second column indicates uncertainties in bottom-up reported emissions (e.g. due to the temporal interpolation) and the presence of other uncertainties in the emission estimation which were not considered. These include the simplified representation of instrument noise, wind speed, and AMF correction. On top of these random errors,

there are uncertainties due to systematic errors such as the estimation of background concentrations, the application of the
305 NO_2 -to- NO_x conversion factors to annual data, and methodological uncertainties, which are not represented in the estimated
uncertainties.

The third column in Table 4 shows the uncertainties in annual emissions according to error propagation, while the fourth
column additionally accounts for uncertainties in diurnal and seasonal cycles.

Table 4. Uncertainties of NO_x emission estimates for single-overpass and annual estimates for Bełchatów, Jänschwalde, Lipetsk, and Ma-
timba

Source	Single-overpass estimates [%]		Annual estimates [%]	
	Median uncertainty	SD of bottom-up - estimated NO_x	Spline uncertainty	Total uncertainty
Bełchatów	23.2	41.7	5.9	9.5
Jänschwalde	24.0	4.6	14.4	20.5
Lipetsk	20.5	–	6.9	10.6
Matimba	25.8	46.3	1.6	3.9

A simple sensitivity analysis in which the NO_2 -to- NO_x conversion factors of Jänschwalde and Matimba were applied to all
310 four sources resulted in emission estimates ranging from 10% lower to 50% higher than the estimates shown in Fig. 7. This
illustrates that the parameterisation of the conversion of NO_2 to NO_x depends on the specific situation such as meteorological
conditions, background concentrations, and emission strength, and not representing this situation appropriately adds a signif-
icant uncertainty to the emission estimates. To get a better understanding of these uncertainties, it would be necessary to run
more high-resolution chemistry transport simulations covering a wider range of conditions, and to account for these conditions
315 in an extended parameterisation. These simulations could be used to generate a look-up table for the NO_2 -to- NO_x conversion
parameters for different conditions. Despite its simplicity, the first-order parameterisation proposed here, which builds on a
small set of high-resolution MicroHH simulations for each source, already leads to a substantial reduction of the bias.

4 Discussion

4.1 Strengths and weaknesses of the time-dependent conversion of NO_2 to NO_x

320 The analysis of $\text{NO}_x:\text{NO}_2$ ratios in modelled plumes demonstrated the importance of chemical processes leading to a general
decrease of this ratio with distance from the source but it also revealed considerable variability from case to case, which is
likely the result of different amounts of emitted quantities, background concentrations, temperatures, wind and turbulent mixing
conditions. The aim of the time-dependent algorithm developed in this study is to reproduce the NO_2 to NO_x conversion of
line densities along the plume (Figure 1). If the true chemistry is well approximated, this should lead to a good agreement with
325 the prescribed emissions. The remaining discrepancy is therefore due to deviations from our simplified assumptions (e.g. the
assumption of an exponential decay of the ratios along the plume) and due to uncertainties in the CSF method. One important

source of uncertainty in the CSF method is the wind speed used to convert line densities to fluxes, which is discussed in section 4.3. The errors of the time-dependent algorithm are more in line with those of the modelled NO_x fields but are slightly larger because the implemented conversion of NO_2 to NO_x does not take into account the specific meteorological and background conditions of each time step, but is based on the median conditions. Thus, the bias is likely to increase when the NO_2 -to- NO_x conversion factors derived in this study are applied to annual data, as the chemical and meteorological conditions vary considerably during a year. Nevertheless, we argue that applying the four fitted NO_2 -to- NO_x conversion functions to annual TROPOMI images yields suitable emission estimates because most of the images that can be used for plume detection were acquired between April and October (see Figure A3). Images taken during the rest of the year often cannot be used for NO_x estimation due to high cloud cover. Consequently, the prevailing conditions for most of the emission estimates are comparable to the conditions in the MicroHH model simulations, which represent days in May to July. This is supported by Figure A7 which shows that the simulated wind speeds of the time steps used for the analysis at the source locations are within the interquartile range of ERA-5 wind speeds for the same locations for the years 2020 and 2021. As the newly implemented conversion function for NO_2 to NO_x showed a significant improvement in the estimation of NO_x emissions and lifetimes from MicroHH simulations, we consider it suitable for the application to TROPOMI images.

4.2 Quantification of NO_x emissions using TROPOMI observations

The application of the time-dependent conversion of NO_2 to NO_x to the TROPOMI data in Figure 7 has shown that the NO_x emission estimates obtained with the time-dependent algorithm are much closer to the bottom-up reported emissions than the estimates from the algorithm with a constant NO_2 -to- NO_x conversion factor of 1.32. The relative median bias is reduced from between -50 and -42% to only between -9.5 to -0.5% . However, the significant variance in estimated emissions for Matimba indicates the necessity for further refinement of the approach. One improvement would be to investigate very long plumes that have been subject to different meteorological conditions than those under which the NO_2 -to- NO_x conversion factors were derived.

As the number of successful emission estimates per year has a strong influence on the uncertainties of the annual emission estimates, maximising the number of suitable satellite images is crucial. Nevertheless, only a fraction of the TROPOMI images could be used for Bełchatów, Jänschwalde, and Lipetsk due to cloud cover. Especially between October and February, emissions could only be estimated for a few days (see Figure A3). The strong seasonal bias in the number of successful estimates may lead to an underestimation of annual emissions as emissions in winter are expected to be larger due to the higher demand of electricity and heating. This gap cannot be filled by the upcoming polar-orbiting Sentinel-5 satellite either but could be alleviated by existing and upcoming geostationary satellites such as GEMS, TEMPO, and Sentinel-4: The hourly temporal resolution increases the probability of obtaining a usable image on a cloudy day. Multiple images during a day would also allow to resolve the diurnal cycle of NO_x emissions, which currently cannot be captured with only one or two overpasses around noon. However, GEMS, Sentinel-4, and -5 have a coarser resolution compared to Sentinel-5P. The complications caused by a coarse spatial resolution can be seen in the example of Jänschwalde: As there are two coal-fired power plants in the vicinity of Jänschwalde (e.g., the Boxberg and Schwarze Pumpe power plants), the plumes often mix, which is why the

emissions cannot be estimated reliably using the CSF method. This applies to a lesser extent to Bełchatów. In contrast, fewer sources that could lead to overlapping plumes are located around Lipetsk and Matimba. As shown in Kuhlmann et al. (2021), a satellite with higher spatial resolution, such as CO2M, can help to better differentiate between plumes, mitigating the challenge of overlapping plumes.

365 The comparison of the uncertainties of the NO_x emission estimates in this study with those in Kuhlmann et al. (2021) highlights the importance of the number of successful emission estimates. The uncertainties of the annual emissions of 4 to 21% in this study are significantly lower than the uncertainties of 16 to 73% and 13 to 52% for two and three of the CO2M satellites in Kuhlmann et al. (2021). The reasons are the higher temporal resolution of TROPOMI compared to CO2M and the high source strength of the power plants considered in the current study. The single-overpass estimates due to random error, 370 in contrast, are only marginally lower in this study than the 29% derived in Kuhlmann et al. (2021). This difference may be attributed to the consideration of additional uncertainties in their study by including a source strength dependent factor and an offset.

The systematic biases due to the application of the NO_2 -to- NO_x conversion factors to annual TROPOMI data were investigated in the form of a sensitivity analysis. Applying the NO_2 -to- NO_x conversion factors of Jänschwalde and Matimba to all 375 four sources resulted in emission estimates ranging from 10% lower to 50% higher, which illustrates that the parameterisation of the conversion of NO_2 to NO_x still adds a significant but unknown uncertainty to the emission estimates. This is because it is not possible to determine how well the conditions under which these parameterisations were derived match those of a given TROPOMI image. However, since most of the suitable satellite images are from the season for which the MicroHH simulations were run, we argue that the calculated NO_2 -to- NO_x conversion factors are likely to be in good agreement with the conditions 380 of the TROPOMI images.

Overall, the application of the newly developed NO_2 -to- NO_x conversion factors resulted in more accurate emission estimates compared to the previous constant conversion factor of 1.32. Nevertheless, extrapolating the conversion factors for different meteorological and background conditions remains a challenge.

4.3 Effective wind speeds in plumes

385 Apart from the NO_x chemistry, a realistic representation of the effective wind speed at which the plume is transported is a key issue. This includes the vertical averaging of 3D wind fields and the consideration of time-varying wind fields. To address the first challenge, the 3D wind speeds were weighted with the expected emission profiles. An advantage of this method is that the weighted winds correspond better to the plume when it is not yet well-mixed within the PBL, i.e. close to the source or in a stably stratified atmosphere. However, with increasing distance from the source, the trace gases become progressively more 390 well-mixed within the PBL. Depending on meteorological conditions, homogeneous mixing can occur within the first few kilometres of the plume (Krol et al., 2024). In such cases, it would be more reasonable to use the mean wind speed within the PBL. Furthermore, Brunner et al. (2019) have shown that plumes typically rise to a height of 250 m in winter, but up to 360 m in summer. Winds are strongly influenced by the dynamics of the PBL, which has a distinct diurnal cycle, especially in summer. These results suggest that a fixed emission profile is likely not sufficient to vertically weigh the 3D wind fields. Instead, the

395 effective wind should be calculated dynamically and account for parameters such as stack height, flue gas properties, and meteorological conditions (Brunner et al., 2019). On the bottom line, further studies are needed to assess the suitability of this method to vertically average the wind speeds under different conditions.

4.4 Impact of air mass factors

The coarse resolution of the a priori NO₂ profiles used for the retrieval of NO₂ VCDs leads to an underestimation of VCDs within the plume and an overestimation outside. As the NO₂ background VCDs are subtracted from the plume enhancements, 400 updating the NO₂ profiles both within and outside the plume would further increase NO_x emission estimates. This would lead to higher emission estimates and possibly an overestimation which would be in line with the slight overestimation of NO_x emissions when using the time-dependent algorithm in Figure 6 for the same reasons as discussed in section 3.1.

Ideally, the a priori NO₂ profiles of the TM5-MP model should be replaced by profiles from higher resolution models such as GEM-MACH (Goldberg et al., 2019b) or CAMS-regional (Douros et al., 2023). However, updating the AMFs for all pixels was beyond the scope of this study. For this reason, the a priori NO₂ profiles of plume pixels were replaced by a constant NO₂ mole fraction of $5 \cdot 10^{-9}$ mol/mol within the PBL. This resulted in lower AMFs and consequently higher VCDs by a factor of 1.15 to 1.35. Other studies have calculated significantly larger corrections. For example, Beirle et al. (2019) found that the VCD excess needs to be corrected by a factor of 1.35 for South Africa and 1.98 for Germany. The higher values are attributed 410 to the assumption made by Beirle et al. (2019) that the entire plume is confined between 60 and 200 m above ground level, where the height-resolved AMFs are typically smaller than at higher altitudes. In contrast, the correction factors in this study were calculated assuming a homogeneous distribution within the PBL, which is more realistic and in line with the MicroHH simulations. Douros et al. (2023) analysed the impact of replacing the TROPOMI a priori NO₂ profiles over Europe with data from the higher resolution CAMS-regional model at a resolution of $0.1 \times 0.1^\circ$. They found that the NO₂ VCDs increased by 415 a factor of 1.05 for less polluted sites and up to 1.3 for more polluted sites which is in good agreement with the increases in VCDs calculated in this study. We conducted a sensitivity study with the MicroHH profiles of Matimba to assess the impact of varying NO₂ profiles inside the plume, showing that the use of the AMF calculated when assuming constant NO₂ PBL concentrations to convert SCDs to VCDs leads to an underestimation of 8.5% compared to when using the true MicroHH NO₂ VCDs (see Figure S5 in the supplement).

4.5 Bottom-up reported emissions

In this study, knowledge of bottom-up reported NO_x and CO₂ emissions is important for two reasons. Firstly, they are used to evaluate the accuracy of the estimated NO_x emissions from satellites. Secondly, reported emissions can be used to convert the estimated NO_x emissions into CO₂. For both applications it is crucial to have information on the reliability and accuracy of the bottom-up reported emissions. However, many of the bottom-up reported CO₂ emissions are estimated from fuel consumption, 425 making assumptions about combustion efficiency, fuel purity and other factors, introducing many uncertainties which are difficult to quantify (IPCC, 2006). It is assumed that bottom-up uncertainties for CO₂ are in the range of $\pm 10\%$ (Gurney et al., 2016) but significantly higher for NO_x (e.g., Zhao et al., 2011). Deviations between estimated and bottom-up reported

emissions are therefore not necessarily due to errors in the estimates but could also originate from inaccuracies in the reported emissions.

430 5 Conclusions

In this study, we derived a more realistic model for the conversion of NO_2 to NO_x in plumes of large NO_x sources. We derived parameters for this model using high-resolution chemistry transport model simulations. The conversion model was then applied to TROPOMI observations from 2020 and 2021.

The results show that annual NO_x emissions can be reliably estimated with TROPOMI: the discrepancies between bottom-up
435 and top-down estimates were reduced from between -50 and -42% to only between -9.5 to -0.5% with uncertainties ranging from 4 to 21%. These more accurate NO_x emission estimates are important for air quality monitoring and can be used to convert NO_x to CO_2 emissions using $\text{CO}_2:\text{NO}_x$ emission ratios, allowing the use of NO_2 imaging satellites such as GEMS, TEMPO, Sentinel-4, and -5 to estimate CO_2 emission with high temporal resolution. Furthermore, geostationary satellites will allow to better resolve the diurnal cycle of emissions and could help to reduce a potential seasonal bias by reducing the number
440 of failed emission estimates caused by cloud cover.

This study also highlights several shortcomings of the current approach. More comprehensive and systematic studies are necessary to determine the dependence of the NO_2 -to- NO_x conversion factor on prevailing conditions such as wind speed, atmospheric stability, solar radiation, temperature, and background concentrations of reactive trace gases. An alternative approach for converting NO_2 into NO_x line densities would be to use machine learning such as neural networks. Once trained
445 with a high-resolution model with chemistry like MicroHH, the network could predict the NO_2 -to- NO_x conversion factors without the need to run a high-resolution chemistry transport model for each plume. However, a large number of simulations covering a wide range of conditions would need to be run for proper training and validation of a machine learning model. Furthermore, we mentioned that more research is necessary to determine how wind speeds should be vertically averaged in plumes and how systematic uncertainties due to AMFs can be best accounted for.

The time-dependent NO_2 -to- NO_x conversion model has been implemented in *ddeq* and can be adjusted for different sources
450 and conditions. An example Jupyter notebook using Python provides easy access to the implementations, enabling users to estimate NO_x emissions from NO_2 satellite observations of specific sources using their own set of NO_2 -to- NO_x conversion parameters. These emissions can then be converted to CO_2 emissions using $\text{CO}_2:\text{NO}_x$ ratios. Therefore, the current study is an important step towards consistent, uniform, high-resolution, and near real-time estimation of NO_x and CO_2 emissions with
455 the use of satellites, which is crucial for air quality monitoring and greenhouse gas emission monitoring and verification.

Code and data availability. The *ddeq* version 1.0 used for this study is available available on Gitlab.com (<https://gitlab.com/empa503/remote-sensing/ddeq>). MicroHH data can be downloaded on Zenodo (Koene and Brunner, 2022). An example notebook on how to use the conversion of NO_2 to NO_x covered in this paper can be found in the supplement.

Appendix A: Additional figures

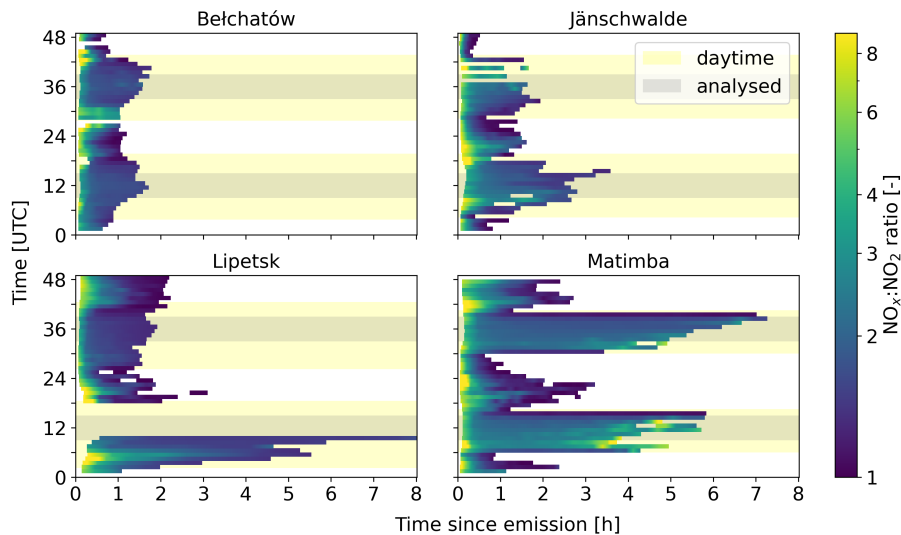


Figure A1. $\text{NO}_x:\text{NO}_2$ ratios for 48 individual hourly time steps of the MicroHH simulations of Belchatów, Jänschwalde, Lipetsk, and Matimba as a function of time since emission, highlighting the spatiotemporal patterns of the NO_x chemistry. Yellow shading represents daytime and grey shading represents the time steps used in the analysis.

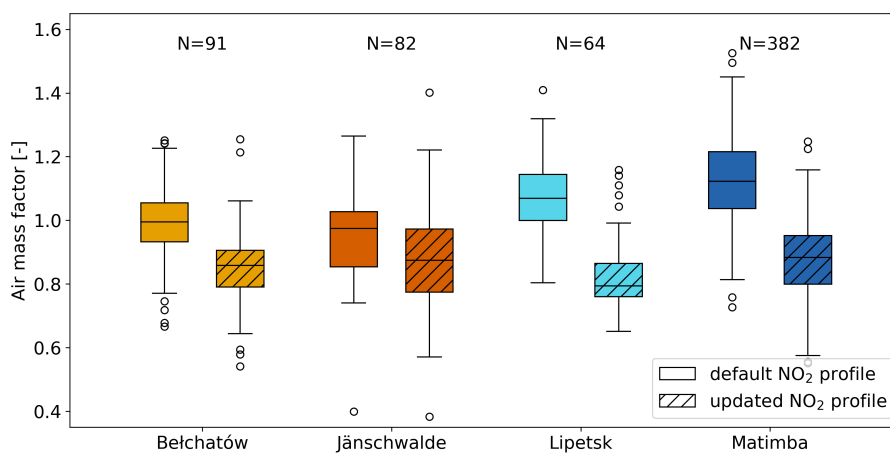


Figure A2. Default and updated AMF of TROPOMI images of Belchatów, Jänschwalde, Lipetsk, and Matimba for the years 2020 and 2021. For the updated AMFs, the NO_2 mole fraction was set to $5 \cdot 10^{-9}$ mol/mol within the PBL of the detected plumes

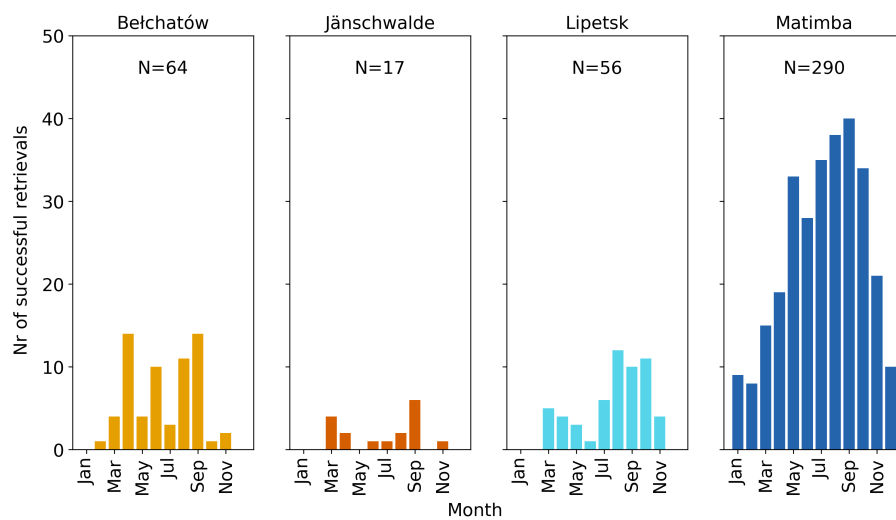


Figure A3. Number of successful NO_x emission estimates per month using TROPOMI for 2020 and 2021

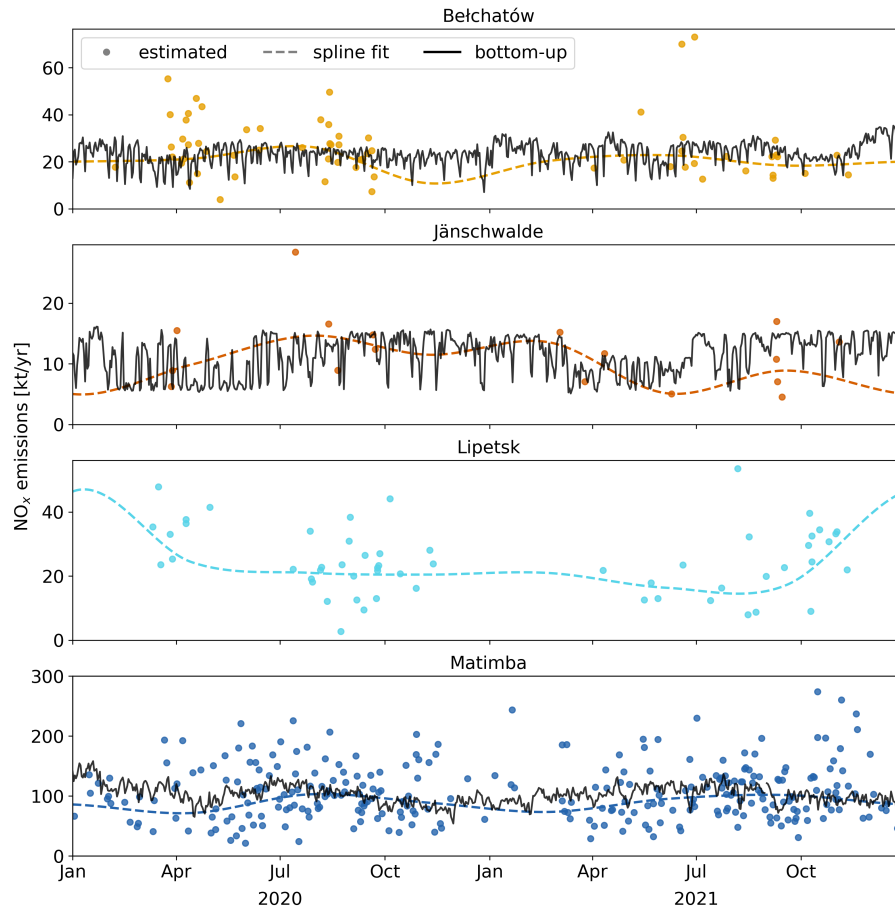


Figure A4. Time series of NO_x emission estimates using TROPOMI and bottom-up reported emissions for the years 2020 and 2021. To each time series, a cubic Hermite spline with periodic boundary conditions was fitted.

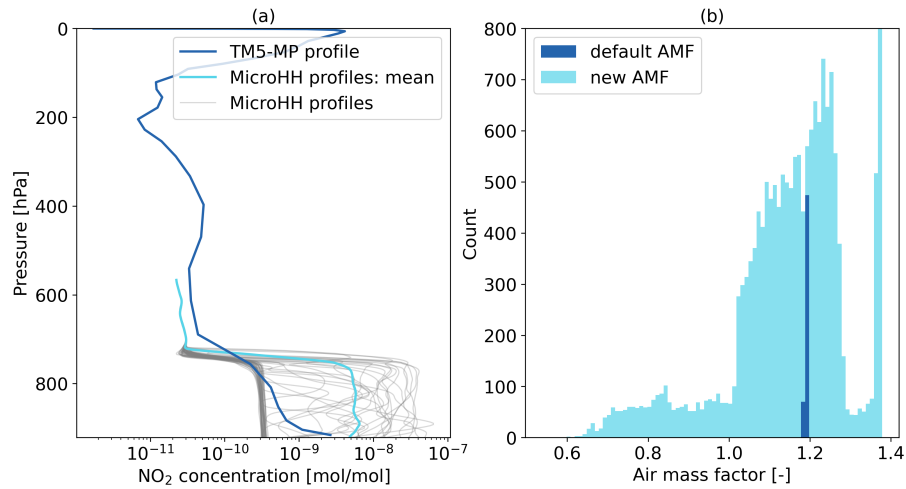


Figure A5. (a) TM5-MP and MicroHH NO₂ profiles of the Sentinel-5P source pixel for Matimba on the 25th of July 2020 at 12:00 UTC. (b) Histogram of the default and recalculated AMFs of the TROPOMI pixel containing the Matimba power plant based on MicroHH NO₂ profiles

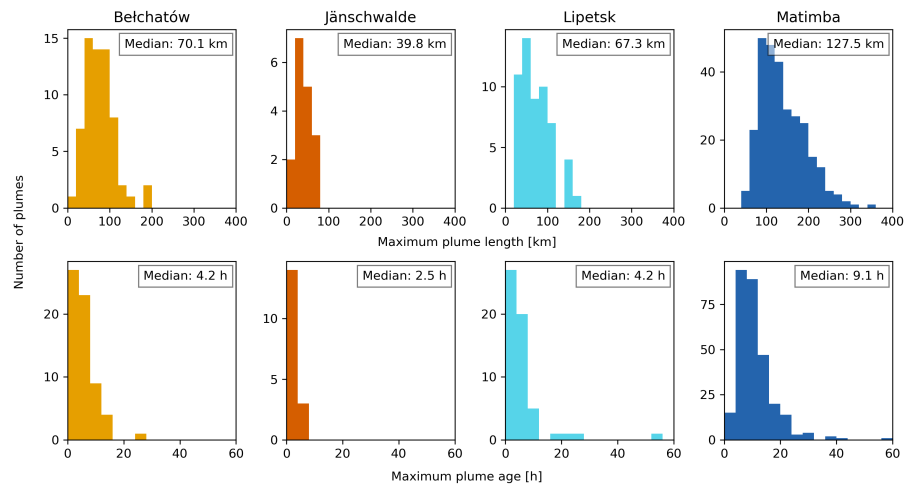


Figure A6. Maximum lengths and ages of detected plumes from TROPOMI observations for the years 2020 and 2021. Ages were calculated by dividing the plume length by the profile weighted wind speed at the source.

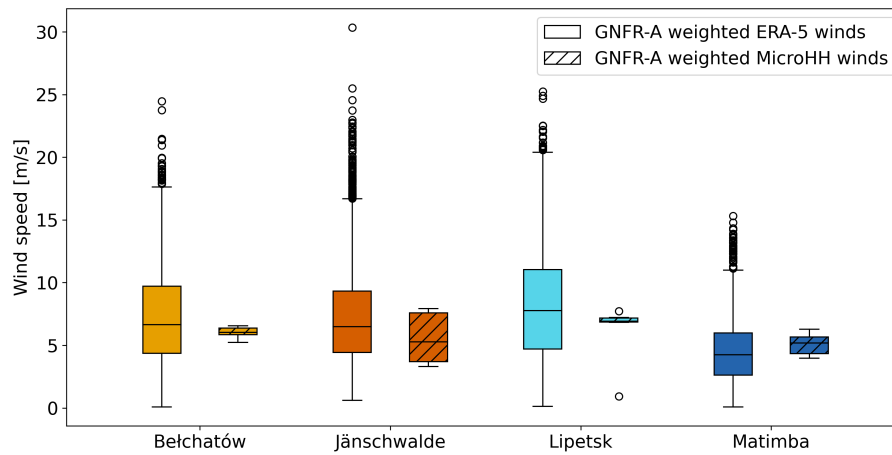


Figure A7. Vertically integrated ERA-5 wind speeds at TROPOMI overpass time for the years 2020 and 2021, and vertically integrated simulated wind speeds in MicroHH for the time steps 8 to 14 UTC on both simulated days. For both variables, the wind speed was sampled at the location of the sources Bełchatów, Jänschwalde, Lipetsk, and Matimba.

460 *Author contributions.* SM conducted the analysis and authored the manuscript with input from all co-authors; EK processed MicroHH
model simulations into pseudo satellite images; MK provided insight in the MicroHH simulations and NO_x chemistry; DB and AD offered
constructive manuscript feedback; GK coordinated and supervised the project.

Competing interests. The authors declare no competing interests.

Acknowledgements. The research was funded by the Horizon Europe CORSO project (no. 101082194) with additional funding by the Swiss
465 State Secretary for Education, Research and Innovation (SERI, no: 22.00422). We like to acknowledge the ICOS Carbon Portal for providing
the computational resources needed for the analysis shown in this paper.

References

- Beirle, S., Boersma, K. F., Platt, U., Lawrence, M. G., and Wagner, T.: Megacity Emissions and Lifetimes of Nitrogen Oxides Probed from Space, *Science*, 333, 1737–1739, <https://doi.org/10.1126/science.1207824>, 2011.
- 470 Beirle, S., Borger, C., Dörner, S., Li, A., Hu, Z., Liu, F., Wang, Y., and Wagner, T.: Pinpointing nitrogen oxide emissions from space, *Science Advances*, 5, <https://doi.org/10.1126/sciadv.aax9800>, 2019.
- Beirle, S., Borger, C., Dörner, S., Eskes, H., Kumar, V., de Laat, A., and Wagner, T.: Catalog of NO_x emissions from point sources as derived from the divergence of the NO₂ flux for TROPOMI, *Earth System Science Data*, 13, 2995–3012, <https://doi.org/10.5194/essd-13-2995-2021>, 2021.
- 475 Bovensmann, H., Buchwitz, M., Burrows, J. P., Reuter, M., Krings, T., Gerilowski, K., Schneising, O., Heymann, J., Tretner, A., and Erzinger, J.: A remote sensing technique for global monitoring of power plant CO₂ emissions from space and related applications, *Atmos. Meas. Tech.*, 3, 781–811, <https://doi.org/10.5194/amt-3-781-2010>, 2010.
- Brunner, D., Kuhlmann, G., Marshal, J., Clément, V., Fuhrer, O., Broquet, G., Löscher, A., and Meijer, Y.: Accounting for the vertical distribution of emissions in atmospheric CO₂ simulations, *Atmospheric Chemistry and Physics*, 19, 4541–4559, <https://doi.org/10.5194/acp-19-4541-2019>, 2019.
- 480 de Foy, B., Lu, Z., Streets, D. G., Lamsal, L. N., and Duncan, B. N.: Estimates of power plant NO_x emissions and lifetimes from OMI NO₂ satellite retrievals, *Atmospheric Environment*, 116, 1–11, <https://doi.org/10.1016/j.atmosenv.2015.05.056>, 2015.
- Douros, J., Eskes, H., van Geffen, J., Boersma, K. F., Compennolle, S., Pinardi, G., Blechschmidt, A.-M., Peuch, V.-H., Colette, A., and Veefkind, P.: Comparing Sentinel-5P TROPOMI NO₂ column observations with the CAMS regional air quality ensemble, *Geoscientific Model Development*, 16, 509–534, <https://doi.org/10.5194/gmd-16-509-2023>, 2023.
- 485 Eskes, H. and van Geffen, J.: Product user manual for the TM5 NO₂, SO₂ and HCHO profile auxiliary support product, Tech. rep., KNMI, 2021.
- Eskes, H., van Geffen, J., Boersma, F., Eichmann, K.-U., Apituley, A., Pedernana, M., Sneep, M., Veefkind, J., and Loyola, D.: Sentinel-5 precursor/TROPOMI Level 2 Product User Manual Nitrogen dioxide, Tech. rep., KNMI, 2022.
- 490 European Parliament and the Council of the European Union: REGULATION (EC) No 166/2006: Establishment of a European Pollutant Release and Transfer Register and amending Council Directives 91/689/EEC and 96/61, 2006.
- Goldberg, D. L., Lu, Z., Oda, T., Lamsal, L. N., Liu, F., Griffin, D., McLinden, C. A., Krotkov, N. A., Duncan, B. N., and Streets, D. G.: Exploiting OMI NO₂ satellite observations to infer fossil-fuel CO₂ emissions from US megacities, *Science of The Total Environment*, 695, 133 805, 2019a.
- 495 Goldberg, D. L., Lu, Z., Streets, D. G., de Foy, B., Griffin, D., McLinden, C. A., Lamsal, L. N., Krotkov, N. A., and Eskes, H.: Enhanced capabilities of TROPOMI NO₂: Estimating NO_x from north american cities and power plants, *Environmental science & technology*, 53, 12 594–12 601, 2019b.
- Goldberg, D. L., Harkey, M., de Foy, B., Judd, L., Johnson, J., Yarwood, G., and Holloway, T.: Evaluating NO_x emissions and their effect on O₃ production in Texas using TROPOMI NO₂ and HCHO, *Atmospheric Chemistry and Physics*, 22, 10 875–10 900, 2022.
- 500 Griffin, D., Zhao, X., McLinden, C. A., Boersma, F., Bourassa, A., Dammers, E., Degenstein, D., Eskes, H., Fehr, L., Fioletov, V., et al.: High-resolution mapping of nitrogen dioxide with TROPOMI: First results and validation over the Canadian oil sands, *Geophysical Research Letters*, 46, 1049–1060, 2019.

- Gurney, K. R., Huang, J., and Coltin, K.: Bias present in US federal agency power plant CO₂ emissions data and implications for the US clean power plan, *Environmental Research Letters*, 11, 064005, 2016.
- 505 Hakkarainen, J., Ialongo, I., Oda, T., Szeląg, M. E., O'Dell, C. W., Eldering, A., and Crisp, D.: Building a bridge: characterizing major anthropogenic point sources in the South African Highveld region using OCO-3 carbon dioxide snapshot area maps and Sentinel-5P/TROPOMI nitrogen dioxide columns, *Environmental Research Letters*, 18, 035003, <https://doi.org/10.1088/1748-9326/acb837>, 2023.
- Hakkarainen, J., Kuhlmann, G., Koene, E., Santaren, D., Meier, S., Krol, M. C., van Stratum, B. J., Ialongo, I., Chevallier, F., Tamminen, J., Brunner, D., and Broquet, G.: Analyzing nitrogen dioxide to nitrogen oxide scaling factors for data-driven satellite-based emission estimation methods: A case study of Matimba/Medupi power stations in South Africa, *Atmospheric Pollution Research*, 15, 102171, <https://doi.org/https://doi.org/10.1016/j.apr.2024.102171>, 2024.
- 510 HERSBACH, H., BELL, B., BERRISFORD, P., BIAVATI, G., HORÁNYI, A., MUÑOZ SABATER, J., NICOLAS, J., PEUBEY, C., RADU, R., ROZUM, I., SCHEPERS, D., SIMMONS, A., SOCI, C., DEE, D., and THÉPAUT, J.-N.: ERA5 hourly data on single levels from 1940 to present, Copernicus Climate Change Service (C3S) Climate Data Store (CDS), <https://doi.org/10.24381/cds.adbb2d47>, 2018.
- 515 Hill, T. and Nassar, R.: Pixel size and revisit rate requirements for monitoring power plant CO₂ emissions from space, *Remote Sensing*, 11, 1608, 2019.
- Huijnen, V., Flemming, J., Chabrilat, S., Errera, Q., Christophe, Y., Blechschmidt, A.-M., Richter, A., and Eskes, H.: C-IFS-CB05-BASCOE: stratospheric chemistry in the Integrated Forecasting System of ECMWF, *Geoscientific Model Development*, 9, 3071–3091, 2016.
- IPCC: 2006 IPCC guidelines for national greenhouse gas inventories, Institute for Global Environmental Strategies, 2006.
- 520 Janssens-Maenhout, G., Pinty, B., Dowell, M., Zunker, H., Andersson, E., Balsamo, G., Bézy, J.-L., Brunhes, T., Bösch, H., Bojkov, B., Brunner, D., Buchwitz, M., Crisp, D., Ciais, P., Counet, P., Dee, D., Denier van der Gon, H., Dolman, H., Drinkwater, M., Dubovik, O., Engelen, R., Fehr, T., Fernandez, V., Heimann, M., Holmlund, K., Houweling, S., Husband, R., Juvyns, O., Kentarchos, A., Landgraf, J., Lang, R., Löscher, A., Marshall, J., Meijer, Y., Nakajima, M., Palmer, P., Peylin, P., Rayner, P., Scholze, M., Sierk, B., Tamminen, J., and Veefkind, P.: Towards an operational anthropogenic CO₂ emissions monitoring and verification support capacity, *Bulletin of the American Meteorological Society*, 0, 1439–1451, <https://doi.org/10.1175/BAMS-D-19-0017.1>, 2020.
- 525 Koene, E. and Brunner, D.: CoCO₂ WP4.1 Library of Plumes, <https://doi.org/10.5281/zenodo.7448144>, 2022.
- Koene, E. and Brunner, D.: D4.2 Assessment of Plume Model Performance, Tech. rep., Empa, <https://coco2-project.eu/node/357>, 2023.
- Krol, M. and van Stratum, B.: D4.1 Definition of simulation cases and model system for building a library of plumes, Tech. rep., WUR, <https://www.coco2-project.eu/node/293>, 2021.
- 530 Krol, M., van Stratum, B., Anglou, I., and Boersma, K. F.: Estimating NO_x emissions of stack plumes using a high-resolution atmospheric chemistry model and satellite-derived NO₂ columns, <https://doi.org/10.5194/egusphere-2023-2519>, manuscript in preparation, 2024.
- Kuhlmann, G., Broquet, G., Marshall, J., Clément, V., Löscher, A., Meijer, Y., and Brunner, D.: Detectability of CO₂ emission plumes of cities and power plants with the Copernicus Anthropogenic CO₂ Monitoring (CO2M) mission, *Atmospheric Measurement Techniques*, 12, 6695–6719, <https://doi.org/10.5194/amt-12-6695-2019>, 2019.
- 535 Kuhlmann, G., Brunner, D., Broquet, G., and Meijer, Y.: Quantifying CO₂ emissions of a city with the Copernicus Anthropogenic CO₂ Monitoring satellite mission, *Atmospheric Measurement Techniques*, 13, 6733–6754, <https://doi.org/10.5194/amt-13-6733-2020>, 2020.
- Kuhlmann, G., Henne, S., Meijer, Y., and Brunner, D.: Quantifying CO₂ Emissions of Power Plants With CO₂ and NO₂ Imaging Satellites, *Frontiers in Remote Sensing*, 2, <https://doi.org/10.3389/frsen.2021.689838>, 2021.

- Kuhlmann, G., Koene, E. F. M., Meier, S., Santaren, D., Broquet, G., Chevallier, F., Hakkarainen, J., Nurmela, J., Amorós, L., Tamminen, J., and Brunner, D.: The ddeq Python library for point source quantification from remote sensing images (Version 1.0), accepted in *Geo. Mod. Dev.*, <https://doi.org/10.5194/egusphere-2023-2936>, 2024.
- Lange, K., Richter, A., and Burrows, J. P.: Variability of nitrogen oxide emission fluxes and lifetimes estimated from Sentinel-5P TROPOMI observations, *Atmospheric Chemistry and Physics*, 22, 2745–2767, <https://doi.org/10.5194/acp-22-2745-2022>, 2022.
- Liu, F., Duncan, B. N., Krotkov, N. A., Lamsal, L. N., Beirle, S., Griffin, D., McLinden, C. A., Goldberg, D. L., and Lu, Z.: A methodology to constrain carbon dioxide emissions from coal-fired power plants using satellite observations of co-emitted nitrogen dioxide, *Atmospheric Chemistry and Physics*, 20, 99–116, 2020.
- Lorente, A., Boersma, K., Eskes, H., Veeffkind, J., van Geffen, J., De Zeeuw, M., Denier van Der Gon, H., Beirle, S., and Krol, M.: Quantification of nitrogen oxides emissions from build-up of pollution over Paris with TROPOMI, *Scientific reports*, 9, 20033, 2019.
- Nassar, R., Hill, T. G., McLinden, C. A., Wunch, D., Jones, D. B. A., and Crisp, D.: Quantifying CO₂ Emissions From Individual Power Plants From Space, *Geophysical Research Letters*, 44, 10,045–10,053, <https://doi.org/10.1002/2017GL074702>, 2017.
- Nassar, R., Moeini, O., Mastrogiacomo, J.-P., O'Dell, C. W., Nelson, R. R., Kiel, M., Chatterjee, A., Eldering, A., and Crisp, D.: Tracking CO₂ emission reductions from space: A case study at Europe's largest fossil fuel power plant, *Frontiers in Remote Sensing*, 3, <https://doi.org/10.3389/frsen.2022.1028240>, 2022.
- Pinty, B., Janssens-Maenhout, G., Dowell, M., Zunker, H., Brunhe, T., Ciais, P., Dee, D., van der Gon, H. D., Dolman, H., Drinkwater, M., Engelen, R., Heimann, M., Holmlund, K., Husband, R., Kentarchos, A., Meijer, Y., Palmer, P., and Scholz, M.: An Operational Anthropogenic CO₂ Emissions Monitoring & Verification Support capacity - Baseline Requirements, Model Components and Functional Architecture, Report, European Commission Joint Research Centre, <https://doi.org/10.2760/39384>, 2017.
- Pronobis, M.: Reduction of nitrogen oxide emissions, *Environmentally Oriented Modernization of Power Boilers*; Elsevier: Amsterdam, The Netherlands, pp. 79–133, 2020.
- Reuter, M., Buchwitz, M., Schneising, O., Krautwurst, S., O'Dell, C. W., Richter, A., Bovensmann, H., and Burrows, J. P.: Towards monitoring localized CO₂ emissions from space: co-located regional CO₂ and NO₂ enhancements observed by the OCO-2 and S5P satellites, *Atmospheric Chemistry and Physics*, 19, 9371–9383, <https://doi.org/10.5194/acp-19-9371-2019>, 2019.
- Rey-Pommier, A., Chevallier, F., Ciais, P., Broquet, G., Christoudias, T., Kushta, J., Hauglustaine, D., and Sciare, J.: Quantifying NO_x emissions in Egypt using TROPOMI observations, *Atmospheric Chemistry and Physics*, 22, 11 505–11 527, 2022.
- Seinfeld, J. H. and Pandis, S. N.: *Atmospheric chemistry and physics: from air pollution to climate change*, John Wiley & Sons, 2016.
- Thurston, G. D.: Outdoor Air Pollution: Sources, Atmospheric Transport, and Human Health Effects, in: *International Encyclopedia of Public Health (Second Edition)*, edited by Quah, S. R., pp. 367–377, Academic Press, Oxford, second edition edn., ISBN 978-0-12-803708-9, <https://doi.org/10.1016/B978-0-12-803678-5.00320-9>, 2017.
- van Geffen, J., Eskes, H., Boersma, K., and Veeffkind, J.: TROPOMI ATBD of the total and tropospheric NO₂ data products, Tech. rep., KNMI, 2019.
- van Geffen, J., Eskes, H., Compernelle, S., Pinardi, G., Verhoelst, T., Lambert, J.-C., Sneep, M., Ter Linden, M., Ludewig, A., Boersma, K. F., et al.: Sentinel-5P TROPOMI NO₂ retrieval: impact of version v2. 2 improvements and comparisons with OMI and ground-based data, *Atmospheric Measurement Techniques*, 15, 2037–2060, 2022.
- van Heerwaarden, C. C., van Stratum, B. J., Heus, T., Gibbs, J. A., Fedorovich, E., and Mellado, J. P.: MicroHH 1.0: A computational fluid dynamics code for direct numerical simulation and large-eddy simulation of atmospheric boundary layer flows, *Geoscientific Model Development*, 10, 3145–3165, 2017.

- van Stratum, B., van Heerwaarden, C. C., and de Arellano, J. V.-G.: The Benefits and Challenges of Downscaling a Global Reanalysis with Doubly-Periodic Large-Eddy Simulations, *Authorea Preprints*, 2023.
- 580 Varon, D. J., Jacob, D. J., McKeever, J., Jervis, D., Durak, B. O. A., Xia, Y., and Huang, Y.: Quantifying methane point sources from fine-scale satellite observations of atmospheric methane plumes, *Atmospheric Measurement Techniques*, 11, 5673–5686, <https://doi.org/10.5194/amt-11-5673-2018>, 2018.
- 585 Veefkind, J., Aben, I., McMullan, K., Förster, H., de Vries, J., Otter, G., Claas, J., Eskes, H., de Haan, J., Kleipool, Q., van Weele, M., Hasekamp, O., Hoogeveen, R., Landgraf, J., Snel, R., Tol, P., Ingmann, P., Voors, R., Kruizinga, B., Vink, R., Visser, H., and Levelt, P.: TROPOMI on the ESA Sentinel-5 Precursor: A GMES mission for global observations of the atmospheric composition for climate, air quality and ozone layer applications, *Remote Sensing of Environment*, 120, 70–83, <https://doi.org/10.1016/j.rse.2011.09.027>, the Sentinel Missions - New Opportunities for Science, 2012.
- Verhoelst, T., Compernelle, S., Pinardi, G., Lambert, J.-C., Eskes, H. J., Eichmann, K.-U., Fjæraa, A. M., Granville, J., Niemeijer, S., Cede, A., et al.: Ground-based validation of the Copernicus Sentinel-5p TROPOMI NO₂ measurements with the NDACC ZSL-DOAS, MAX-DOAS and Pandonia global networks, *Atmospheric Measurement Techniques*, 14, 481–510, 2021.
- 590 Zhao, Y., Nielsen, C. P., Lei, Y., McElroy, M. B., and Hao, J.: Quantifying the uncertainties of a bottom-up emission inventory of anthropogenic atmospheric pollutants in China, *Atmospheric Chemistry and Physics*, 11, 2295–2308, 2011.